

# N,P-co-doped 2D Carbon Nanosheets for High Energy Density Zinc-Ion Capacitors

Jiaxin Li,<sup>[a]</sup> Yanshen Gao,<sup>[a]</sup> Rudolf Holze,<sup>[b, c, d]</sup> Shiyun Li,<sup>\*[e]</sup> Ewa Mijowska,<sup>[a]</sup> and Xuecheng Chen<sup>\*[a]</sup>

Zinc-ion capacitors (ZICs) are regarded as highly promising candidates for electrical energy storage systems (EESs). However, some challenges must be met to achieve high energy density and long cycling life in practical applications. Herein, we report on design and preparation of 2D nanosheets of N,P-co-doped hierarchical porous carbon (GNPCs) by a one-step process. Benefiting from the mesopores supporting rapid diffusive ion transport, sufficient micropores for charge storage, and high electrical conductivity enabled by N,P-doping, the

resulting GNPC cathodes for ZICs achieved a high capacity of  $401 \text{ Fg}^{-1}$ . In a complete device a high energy density of  $180 \text{ Wh kg}^{-1}$  was obtained at a power density of  $85 \text{ W kg}^{-1}$  at  $0.1 \text{ A g}^{-1}$ . More importantly, the ZICs exhibit a good cycling stability with a capacity retention of 95% after 10 000 cycles at a current density of  $5 \text{ A g}^{-1}$ . Our work presents a good strategy for developing high-performance carbon-based cathodes for ZICs.

## Introduction

Responding to increasing awareness of climate change, many strategies have been proposed to develop cost-effective and safe sustainable EESs. In contrast to the already established lithium-ion batteries (LIBs), Zinc-ion capacitors (ZIC) are promising candidates for power grid applications and portable electronics.<sup>[1]</sup> Typically, ZICs consist of a Zn-based anode, onto which zinc is electrodeposited and dissolved, and a capacitive porous carbon cathode operating with a fast physical adsorption/desorption mechanism. Therefore, ZICs offer intrinsic high safety, high reversibility, as well as no toxicity and environmental compatibility.<sup>[2]</sup> Moreover, the highly abundant metallic zinc could deliver high theoretical capacity

( $820 \text{ mAh g}^{-1}$ ), and a low redox potential of  $-0.76 \text{ V}$  (vs. standard hydrogen electrode), which could possibly address the issues of low power density and safety concerns of LIBs.<sup>[3]</sup> However, ZICs still suffer from low capacity, poor cycling stability and inferior energy density due to the employed carbon cathodes, mainly limited by the sluggish kinetics of Zn-ions within the porous carbon.<sup>[4]</sup>

Recently, biomass-based porous carbon materials have drawn great attention especially as electrode materials for ZICs,<sup>[5]</sup> because they are derived from renewable, low-cost and ample natural sources.<sup>[6]</sup> However, they still face considerable limitations in energy storage, in particular poor electrochemical kinetics, poor cycling life and limited mass transport, which is caused by imperfect pore size distributions and low specific surface area.<sup>[7]</sup> In addition, heteroatoms are difficult to dope into carbon skeletons uniformly to tailor their electronic structure, which could provide more active sites to improve the charge storage capability of electrode materials.<sup>[8]</sup> Thus, a facile and effective strategy that allows easy control of the nano-structure and introduces heteroatoms into the carbon skeleton and yields materials which meet the requirements for cathode materials with a high  $\text{Zn}^{2+}$  storage capacity and superior cycling stability, is vital.<sup>[9]</sup>

Herein, N,P-co-doped 2D nanosheets with hierarchical porous carbon architecture are designed and prepared by a one-step process. During the pyrolysis phosphine from the chamber atmosphere decomposed from sodium hypophosphite ( $\text{NaH}_2\text{PO}_2$ ) in the confined space serves as both activation agent and P-source in the presence of a nitrogen source (melamine) with the glucose carbon sources.<sup>[10]</sup> Its well-designed hierarchical pores can produce a large specific surface area and effective channels for fast electrolyte transport, and the introduced N,P-dopants favor the chemical adsorption of Zn ions.<sup>[1,11]</sup> The ZICs assembled with GNPC cathode display a specific capacity of  $401 \text{ Fg}^{-1}$ , and a high energy density of  $180 \text{ Wh kg}^{-1}$  at a power density of  $85 \text{ W kg}^{-1}$  at  $0.1 \text{ A g}^{-1}$ . Furthermore, the capacity

[a] J. Li, Y. Gao, Prof. E. Mijowska, Prof. X. Chen  
Faculty of Chemical Technology and Engineering  
West Pomeranian University of Technology, Szczecin  
Piastów Ave. 42, 71-065 Szczecin (Poland)  
E-mail: xchen@zut.edu.pl

[b] R. Holze  
Chemnitz University of Technology  
09107, Chemnitz (Germany)

[c] R. Holze  
Institute of Chemistry  
Saint Petersburg State University  
St. Petersburg, 199034 (Russia)

[d] R. Holze  
State Key Laboratory of Materials-oriented Chemical Engineering  
School of Energy Science and Engineering  
Nanjing Tech University  
Nanjing, 211816, Jiangsu Province (China)

[e] S. Li  
School of Materials Science and Engineering  
Jiangsu University of Science and Technology  
Zhenjiang 212003 (China)  
E-mail: shiyunli@just.edu.cn

 Supporting information for this article is available on the WWW under  
<https://doi.org/10.1002/batt.202300175>

retention is 95% after 10 000 cycles at a current density of  $5 \text{ A g}^{-1}$ . The present work shows a practical way to synthesize N,P-co-doped 2D porous nanosheets from biomass materials for high energy density and long-term cycling stable ZICs.

## Results and Discussion

The morphology and nanostructure of the glucose-derived porous carbon materials were observed with TEM and SEM, results are shown in Figure 1. The glucose was directly carbonized into large bulky and thick sheets with several microns size. When melamine was added as the nitrogen source, the obtained GNC still shows the sheet structure but with some micropores, as shown in Figure 1(c<sub>2</sub>), indicating that melamine favors the formation of micropores.<sup>[12]</sup> After introduction of NaH<sub>2</sub>PO<sub>4</sub>, the obtained P-doped carbon (GPC) shows lamellar structure with some fragmentized thin carbon sheets, Figure 1(d<sub>1</sub>). The presence of mesopores in GPC suggests the

activation capability of the PH<sub>3</sub> gas, which was obtained by decomposition of NaH<sub>2</sub>PO<sub>4</sub> during the thermal process at 300 °C. According to Figure 1(d<sub>2</sub>), the simultaneously furnished additional P source enables uniform doping and creates large mesopores in the carbon material during the subsequent carbonization at 800 °C.<sup>[8,13]</sup> As shown in Figure S1(a–c), with the ratio of NaH<sub>2</sub>PO<sub>4</sub> increased from 2 to 6, the GNPC-X samples showed more defects and mesopores. Finally, the coordinated reaction of melamine and NaH<sub>2</sub>PO<sub>4</sub> was introduced to prepare the hierarchical N,P-co-doped porous carbon, as shown in the Figure 1 (e<sub>1</sub>, e<sub>2</sub>).<sup>[14]</sup> It has been reported, that micropores mainly contribute to capacitance, while mesopores allow storage and movement of electrolyte.<sup>[15]</sup>

N<sub>2</sub> adsorption/desorption was employed to analyze the porosity of the glucose-derived porous carbons. As shown in Figure 1(g), all porous carbon materials show combined I and IV type isotherms, where a H-4 hysteresis loop at relative pressure of  $p/p_0 = 0.4\text{--}0.9$  indicates the presence of mesopores.<sup>[16]</sup> Furthermore, the strong adsorption near the low relative

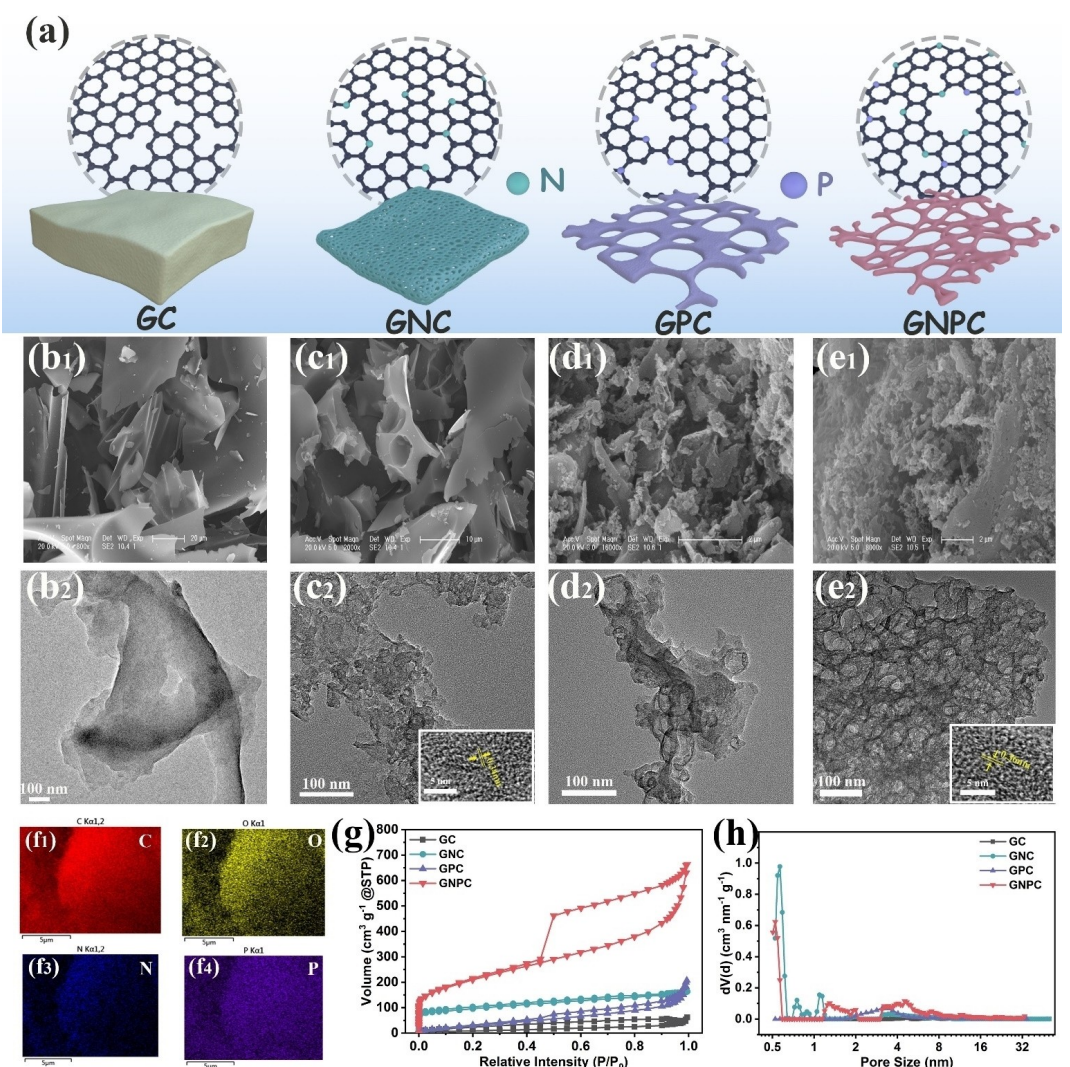


**Figure 1.** a) Schematic illustration of the preparation of GC, GNC, GPC and GNPC. b<sub>1</sub>–e<sub>1</sub>) SEM images and b<sub>2</sub>–e<sub>2</sub>) TEM and HRTEM images of GC, GNC, GPC and GNPC. f) EDX mappings of carbon, oxygen, nitrogen and phosphorus of GNPC; g) N<sub>2</sub> isotherms and h) pore size distributions of glucose derived porous carbon.

pressure region ( $p/p_0 < 0.2$ ) suggests the presence of micropores.<sup>[17]</sup> According to Brunauer-Emmett-Teller (BET) and Density Functional Theory (DFT) calculation analysis GNPC has a specific surface area ( $S_{\text{BET}}$ ) of  $746.7 \text{ m}^2 \text{ g}^{-1}$  and a pore volume ( $V_{\text{total}}$ ) of  $1.03 \text{ cm}^3 \text{ g}^{-1}$ , values much higher than those for GNC ( $S_{\text{BET}} = 340.9 \text{ m}^2 \text{ g}^{-1}$ ,  $V_{\text{total}} = 0.25 \text{ cm}^3 \text{ g}^{-1}$ ) and GPC ( $S_{\text{BET}} = 122.4 \text{ m}^2 \text{ g}^{-1}$ ,  $V_{\text{total}} = 0.67 \text{ cm}^3 \text{ g}^{-1}$ ), as summarized in Table 1. The pore size distribution curves of GNPC show a hierarchical porous structure, where micropores and mesopores were mainly produced from melamine and  $\text{NaH}_2\text{PO}_2$ . The size of micropores is distributed between 0.62 nm and 1.2 nm, while mesopores peak at 4.4 nm (Figure 1h). The mesopores provide

short diffusion channels for the electrolyte transport, and micropores are responsible for the storage of charge.<sup>[8,18]</sup>

The XRD patterns of glucose-derived porous carbon materials show two diffraction peaks at  $2\theta = 23^\circ - 25^\circ$  and  $42^\circ - 43^\circ$  corresponding to the (002) and (101) planes of graphite (Figure 2a). The almost disappearing peak at  $2\theta = 43^\circ$  is attributed to the amorphous structure of GPC with many defects and pores.<sup>[19]</sup> Furthermore, a weak left shift was observed in GNPC, suggesting that N,P-doping can enlarge the graphite lattice layer spacing. As shown in Figure 2(b), in Raman spectra the intensity ratios of  $I_D/I_G$  between disorder D-band ( $\sim 1360 \text{ cm}^{-1}$ ) and graphitized-sp<sup>2</sup> G-band ( $\sim 1600 \text{ cm}^{-1}$ ) for GNC, GPC and GNPC are 0.91, 0.87 and 0.90, lower than GC (1.0), suggesting melamine and  $\text{NaH}_2\text{PO}_2$  can decrease the graphitization degree of glucose-derived carbon.<sup>[20]</sup>

The elemental composition at the surface of GC, GNC, GPC and GNPC was characterized by XPS; results are shown in Figures 2(c) and S2. The GNPC shows 83.73 at.% carbon, 14.57 at.% oxygen, 1.38 at.% nitrogen and 0.32 at.% phosphorus, which agrees well with EDX mapping results (Figure 2e and f). The C 1s can be fitted to  $-\text{C}-\text{C}-$ ,  $-\text{C}=\text{O}$ ,  $\text{O}-\text{C}=\text{O}$  groups at 284.58 eV, 285.88 eV and 288.70 eV. The high-resolution O 1s XPS peak consists of two contributions at 531.93 eV and 533.36 eV, which can be assigned to  $-\text{C}-\text{OH}$  and  $\text{O}-\text{C}=\text{O}$ .

Table 1. Porosity parameters of glucose derived porous carbon materials.				
Sample	$S_{\text{BET}}$ <sup>[a]</sup> [m <sup>2</sup> g <sup>-1</sup> ]	$S_{\text{micro}}$ <sup>[b]</sup> [m <sup>2</sup> g <sup>-1</sup> ]	$V_{\text{total}}$ <sup>[c]</sup> [cm <sup>3</sup> g <sup>-1</sup> ]	Average pore size
GC	33.2	0	0.095	11.45
GNC	340.9	161.9	0.25	0.297
GPC	122.4	0	0.67	0.324
GNPC	746.7	153.4	1.03	5.495

[a] specific surface area was calculated by BET method at  $p/p_0 = 0.003 - 0.1$   
[b] micropore specific surface area obtained from t-plot [c] total pore volume at  $p/p_0 = 0.99$

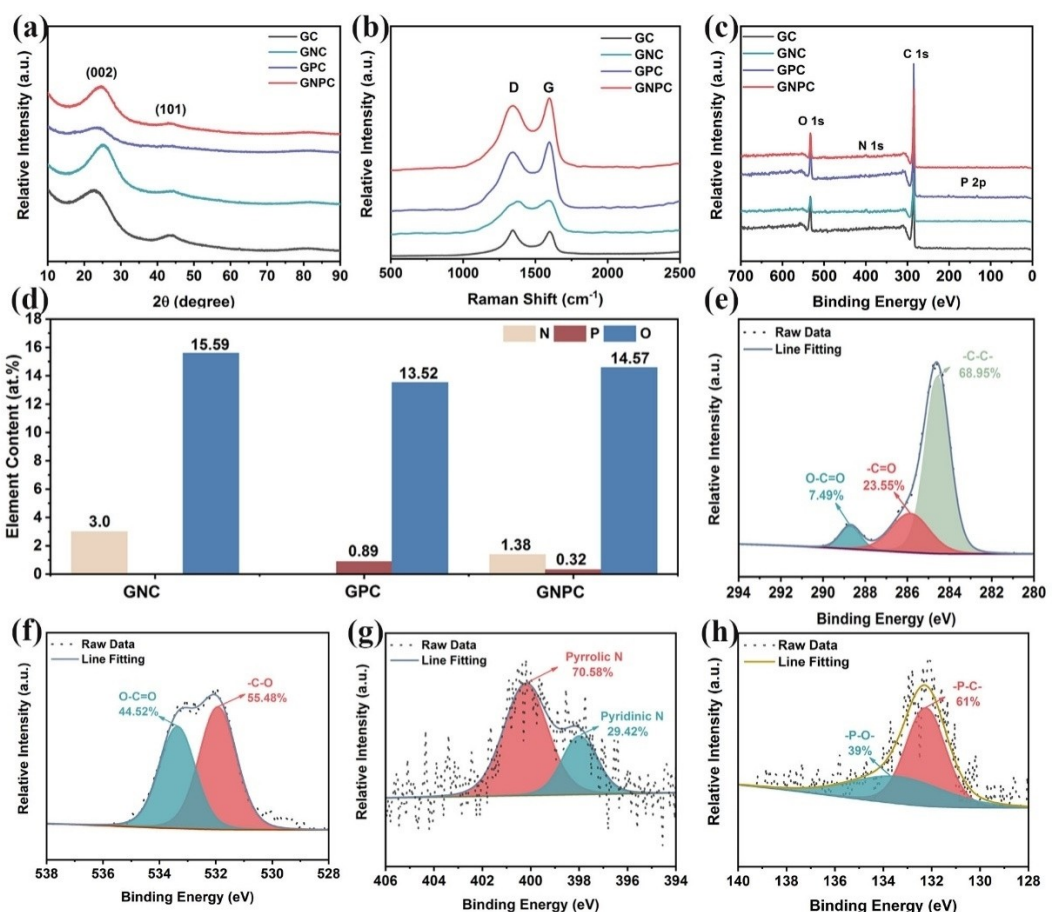
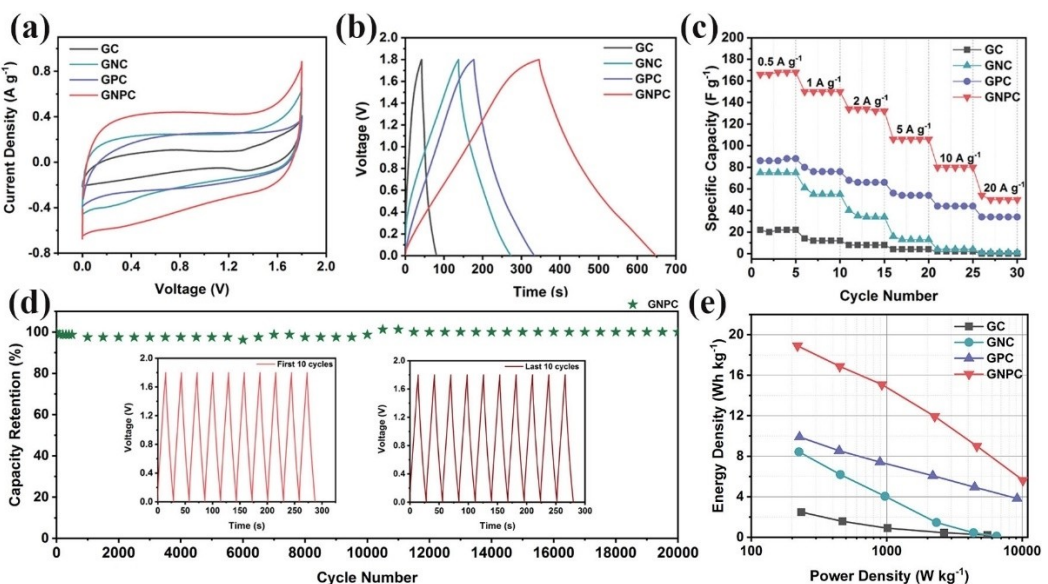


Figure 2. a) XRD patterns; b) Raman spectra and c) XPS survey spectra of glucose-derived porous carbons. d) N/P/O contents of GNC, GPC and GNPC. High-resolution XP spectra of e) C 1s, f) O 1s, g) N 1s and h) P 2p of GNPC.



**Figure 3.** Electrochemical performance of a symmetric supercapacitor with aqueous 1 M  $\text{Li}_2\text{SO}_4$ : a) CV curves at a scan rate of  $5 \text{ mV s}^{-1}$ ; b) GCD curves at  $0.5 \text{ A g}^{-1}$  and c) rate performance at different current densities from  $0.5 \text{ A g}^{-1}$  to  $20 \text{ A g}^{-1}$  of GC, GNC, GPC and GNPC. d) Long term cycling stability of GNPC at a current density of  $5 \text{ A g}^{-1}$  (Inset: first and last 10 cycles before and after 20 000 cycles). e) Ragone plots of the glucose-derived carbon materials.

groups.<sup>[21]</sup> It has been reported that the oxygen groups play an important role in improving the wettability of porous carbon with electrolyte solutions.<sup>[22]</sup> The N 1s spectra of GNPC could be deconvoluted into pyridinic-N (N-6, 397.99 eV) and pyrrolic-N (N-5, 400.21 eV) peaks, shown in Figure 2(g).<sup>[23]</sup> Two types of P-containing groups,  $-\text{P}-\text{C}-$  (132.39 eV) and  $-\text{P}-\text{O}-$  (133.40 eV), are found in the P 2p spectrum. The N,P-co-doped 2D porous nanosheets carbon materials (GNPC) were successfully prepared. It has been reported, that nitrogen-containing groups (N-6 and N-5) and P-sites on their surface are beneficial by favoring chemical interactions between the electrolyte and electrode, boosting the electrochemical performance of capacitors by decreasing the charge transfer resistance due to the improvement of the conductivity.<sup>[24]</sup> As shown in Figure S7, results of contact angle experiments with water for GC and GNPC further prove that GC is hydrophobic and GNPC is hydrophilic, which is also consistent with the above results.

A symmetric supercapacitor was assembled with glucose-derived porous carbon materials and GNPC-X and aqueous 1 M  $\text{Li}_2\text{SO}_4$  (Figures 3 and S3). As presented in Figure 3(a), the nearly rectangular CVs suggest the ideal capacitive behavior of GNPC at a scan rate of  $5 \text{ mV s}^{-1}$ . In Figure S3(e), CVs still maintained a quasi-rectangular shape even at a high scan rate of  $200 \text{ mV s}^{-1}$ , indicating again good capacitive behavior and promising rate performance.<sup>[25]</sup> GCD curves at  $0.5 \text{ A g}^{-1}$  show a typical triangular shape for these porous carbon (GC, GNC, GPC and GNPC), suggesting the effective electric double layer functioning and fast electrolyte transport (Figure 3b).<sup>[26]</sup> A specific capacitance of  $167 \text{ F g}^{-1}$  was achieved for GNPC, higher than that of GNC ( $75 \text{ F g}^{-1}$ ) and GPC ( $87 \text{ F g}^{-1}$ ) at current density of  $0.5 \text{ A g}^{-1}$ . Furthermore, GNPC retained 63.8% of its initial capacity at a current density of  $5 \text{ A g}^{-1}$ , as shown in Figure 3(c). Meanwhile, the long-term cycling stability was measured at  $5 \text{ A g}^{-1}$ , results

are shown in Figure 3(d). The capacity retention is 100% after 20 000 cycles, confirming the structural stability of GNPC. The practical energy storage capability of GNPC is also revealed in a Ragone plot (Figure 3e). The GNPC-based supercapacitor exhibits an energy density of  $18.9 \text{ Wh kg}^{-1}$  at a power density of  $219 \text{ W kg}^{-1}$ , which is higher than that with GNC ( $8.4 \text{ Wh kg}^{-1}$ ;  $225 \text{ W kg}^{-1}$ ) and GPC ( $9.9 \text{ Wh kg}^{-1}$ ;  $227 \text{ W kg}^{-1}$ ).

To get further insights into ion transport kinetics within the electrode, electrochemical impedance spectroscopy (EIS) was applied in a symmetric supercapacitor system.<sup>[27]</sup> In Figure 4(a), all Nyquist plots show a semicircle in the high frequency region and a straight line with  $45^\circ$  slope in the middle-frequency

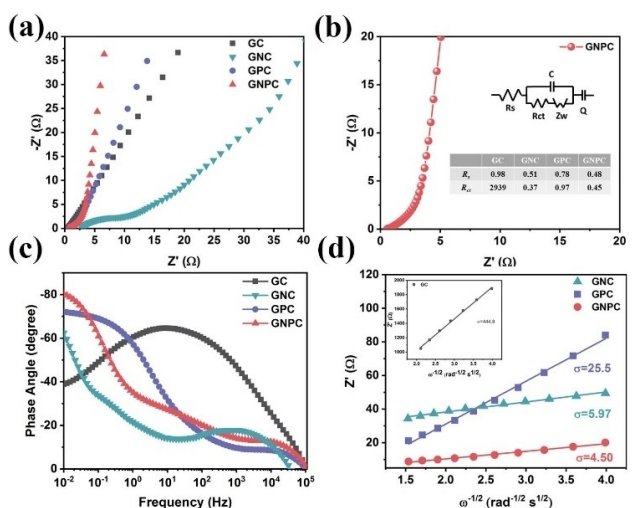


**Figure 4.** a) Nyquist plots; b) equivalent circuit model (inset detailed fitting resistance data table); c) Bode phase angle plot and d) the relationship between  $\omega^{-1/2}$  and  $Z'$  of GC, GNC, GPC and GNPC.

range, which corresponds to the charge transfer resistance ( $R_{ct}$ ) and ion diffusion (Warburg impedance,  $W$ ).<sup>[28]</sup> Commonly, the larger diameter of the semicircle is related to a higher charge transfer resistance ( $R_{ct}$ ) while a smaller slope of the straight line suggests inferior ion diffusion performance. In Figure 4(b), the GNPC presents a semicircle with a smallest radius suggesting its lowest  $R_{ct}$  with minimized charge transfer loss and achieved a high current response. As shown in Figure 4(b), GNPC shows a nearly vertical straight line in the low frequency region, suggesting negligible limitation due to fast ion diffusion.<sup>[29]</sup> The Bode plot (Figure 4c) shows the dependence of phase angle on frequency. The nearly  $-90^\circ$  phase angle of GNPC at low frequency reveals the ideal capacitive behavior, while the smaller time constant ( $\tau_0, \tau_0 = 1/f$ ) at the characteristic of phase angle  $-45^\circ$  suggests its quick response time when releasing the energy accumulated in the device and fast diffusion rate within the porous structure.<sup>[20a,29]</sup> As depicted in Figure 4(d), the values of the slope ( $\sigma$ ) between  $\omega^{-1/2}$  and  $Z'$  plots are 444.8, 5.97, 25.5 and 4.5 for GC, GNC, GPC and GNPC, respectively. According to Equations (7) and (8), the calculated diffusion coefficients of GNPC were about 98, 1.4, and 5.6 times higher than that of GC, GNC and GPC. These results further demonstrate that the N,P-

co-doped porous nanosheet structure and sufficient micro/mesopores that guarantee effective channels for the fast diffusion of electrolyte ions.

To estimate the capacitive performance in a ZIC, the glucose-derived porous carbon materials were assembled with Zn foil in 2 M  $ZnSO_4$  electrolyte, and tested within 0–1.8 V vs.  $Zn^{2+}/Zn$ , results are shown in Figure 5(a). GNPC-114 shows the highest specific capacitance, as well as good rate performance and long-term stability (Figure S4). The GCD presents basically symmetrical data, indicative of high electrochemical reversibility.<sup>[30]</sup> It shows that GNPC has a maximum specific capacity (based on the discharge curve and mass loading) of  $401 \text{ F g}^{-1}$  at  $0.1 \text{ A g}^{-1}$ , higher than that of GC ( $73 \text{ F g}^{-1}$ ), GNC ( $289 \text{ F g}^{-1}$ ) and GPC ( $152 \text{ F g}^{-1}$ ), suggesting enhanced electrochemical performance, as shown in Figure 5(b). Moreover, the GNPC still maintains  $385 \text{ F g}^{-1}$  with 96% retention when the current density returned to  $0.1 \text{ A g}^{-1}$ , proving high robustness, structural stability and rate performance (in Figure 5d). The long-term stability was examined at  $5 \text{ A g}^{-1}$ , results are shown in Figure 5(e). The specific capacity of GNPC retains 95% of its initial value after 10 000 cycles, which is higher than previously reported (Figure 5f). Impressively, as shown in Figure 5(g), the

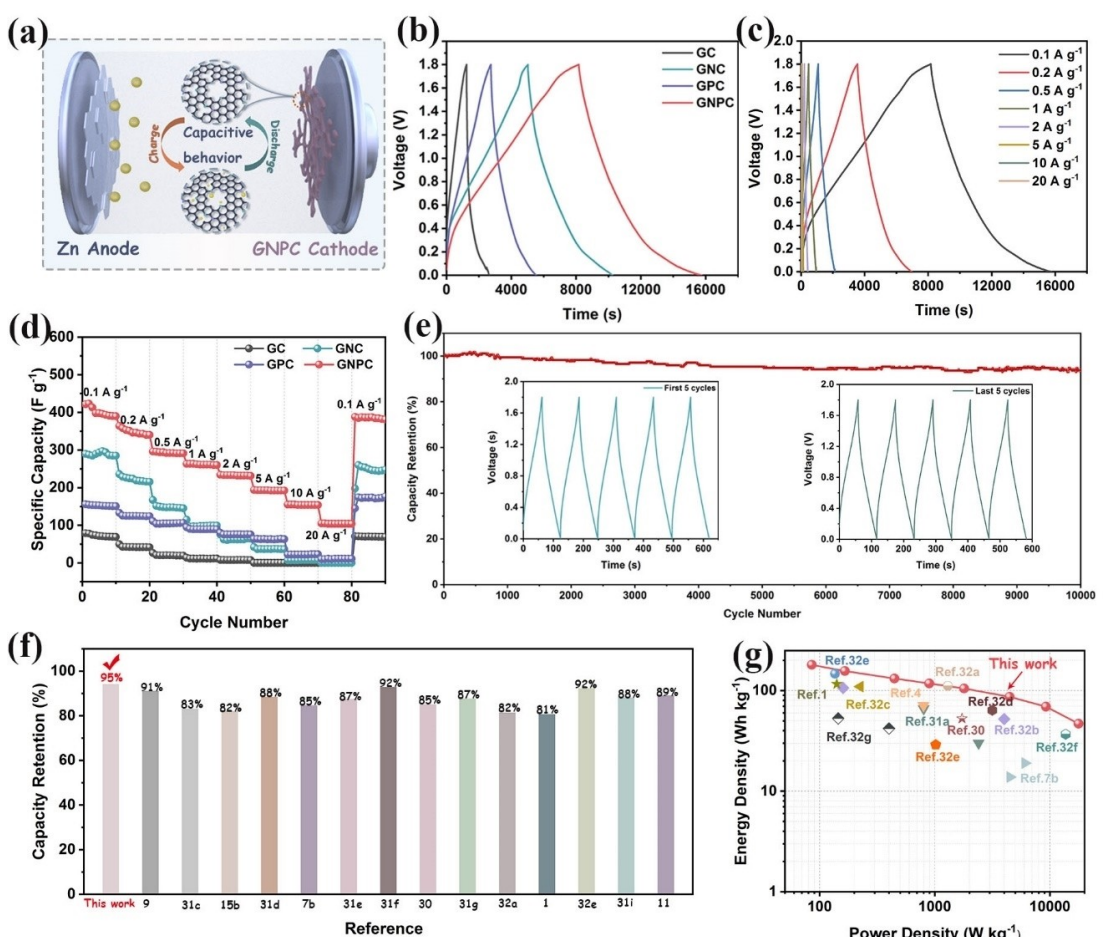


**Figure 5.** a) Schematic illustration of GNPC based ZICs. GCD curves of b) glucose-derived porous carbon at a current density of  $0.1 \text{ A g}^{-1}$  and c) GNPC at various current densities from  $0.1 \text{ A g}^{-1}$  to  $20 \text{ A g}^{-1}$ . d) Rate capability. e) Long term cycling performance of GNPC cathodes at  $5 \text{ A g}^{-1}$  for 10 000 cycles. (Inset: first and last 5 cycles). f) Long-term stability. g) Ragone plot with comparison of reported values of ZIC systems.

GNPC devices presents a high energy density of  $180 \text{ Wh kg}^{-1}$  at a power density of  $85 \text{ W kg}^{-1}$  at  $0.1 \text{ A g}^{-1}$ , which maintains  $46.8 \text{ Wh kg}^{-1}$  at  $17.7 \text{ kW kg}^{-1}$  and  $20 \text{ A g}^{-1}$ , and which is better than that of previously reported carbon-based ZIC devices.

To better understand the electrochemical reaction kinetics of the glucose-derived porous carbon, CVs were further recorded at scan rates from  $1 \text{ mV s}^{-1}$  to  $10 \text{ mV s}^{-1}$  (Figure 6a). The quasi-rectangular curves with reversible oxidation (Peak A) and reduction peaks (Peak B) demonstrate a complex charge storage mechanism, including battery behavior and a capacitive process (Figure 6b).<sup>[7a]</sup> The CVs show little distortion with the increase of the scan rate to  $10 \text{ mV s}^{-1}$ , indicating reversible and fast electrochemical kinetics within the electrodes.<sup>[31e]</sup>

Commonly, the charge storage process can be analyzed by considering current density ( $i$ , mA) and scan rate ( $v$ ,  $\text{mV s}^{-1}$ ) according to the following equations:<sup>[32e]</sup>

$$i(V) = av^b \quad (1)$$

$$\log(i) = \log a + b \log v \quad (2)$$

where  $a$  and  $b$  are adjustable constants.  $b=1$  means that charge storage happens by the surface capacitance, while  $b=0.5$  means it happens by a diffusion-controlled process.<sup>[15b]</sup> Considering the polarization the peak current is chosen rather than the current at the same potential in every cycle. As shown in Figure 6(c), the  $b_A$  and  $b_B$  values of oxidation and reduction

peaks were fitted to be 0.85 and 0.92 at the scan rate of  $1 \text{ mV s}^{-1}$ , suggesting the coexistence of diffusive and capacitive charge storage mechanism at the electrode/electrolyte interface.<sup>[33]</sup>

Moreover, the capacitive and diffusion contribution was investigated quantitatively at different scan rates based on Equation (3)<sup>[1]</sup>

$$i(V) = k_1 v + k_2 v^{1/2} \quad (3)$$

where  $k_1$  and  $k_2$  are constants, and  $k_1 v$  stands for the capacitive controlled contribution and  $k_2 v^{1/2}$  represents the diffusion-controlled process. 37% of the current is provided by the diffusion contribution at a scan rate of  $1 \text{ mV s}^{-1}$ , as shown in Figure 6(d), which provides sufficient time for the electrode to complete the redox reaction.<sup>[6b]</sup> The capacitive contribution percentage gradually increases with the scan rate from  $1 \text{ mV s}^{-1}$  to  $10 \text{ mV s}^{-1}$ . A high capacitive contribution of 85% was achieved while the diffusion-controlled decrease to 15% at  $10 \text{ mV s}^{-1}$ . This verifies fast electrochemical kinetics and a surface capacitive-dominated process of the GNPC device, which benefits from the hierarchically porous structure that offers favorable channels for the storage of Zn ions, in Figure 6(e).<sup>[32c,34]</sup>

The present study demonstrates the enhanced energy storage performance of GNPC based ZICs, as shown schematically in Figure 6(e), which can be attributed to: (i) the gas-steam synthesis strategy enhancing the porosity of the glucose-derived porous carbon, leading to a hierarchical pore size distribution for efficient ion diffusion and storage; (ii) the N,P-doping provides adsorption sites and supports increased electric conductivity for an improved capacity.

## Conclusions

An effective route for the preparation of 2D nanosheets with adjustable pore size distribution and N,P-co-doping is designed and realized in a one-step process. The enhanced porosity originates from its hierarchical nanostructure, where mesopores serve as the effective channels for fast mass transport and storage into micropores. Moreover, N,P-co-doping could further lower the Ohmic resistance of the electrode material between the electrolyte and carbon materials and boost the chemical adsorption of Zn-ions on the electrode surfaces, leading to an enhanced electrochemical performance. Thus, the GNPC-based ZIC delivers a good rate capability and gravimetric capacitance of  $401 \text{ F g}^{-1}$ , a high energy density of  $180 \text{ Wh kg}^{-1}$  under power density of  $85 \text{ W kg}^{-1}$  at  $0.1 \text{ A g}^{-1}$ , as well as a capacity retention of 95% over 10 000 cycles at a current density of  $5 \text{ A g}^{-1}$ .

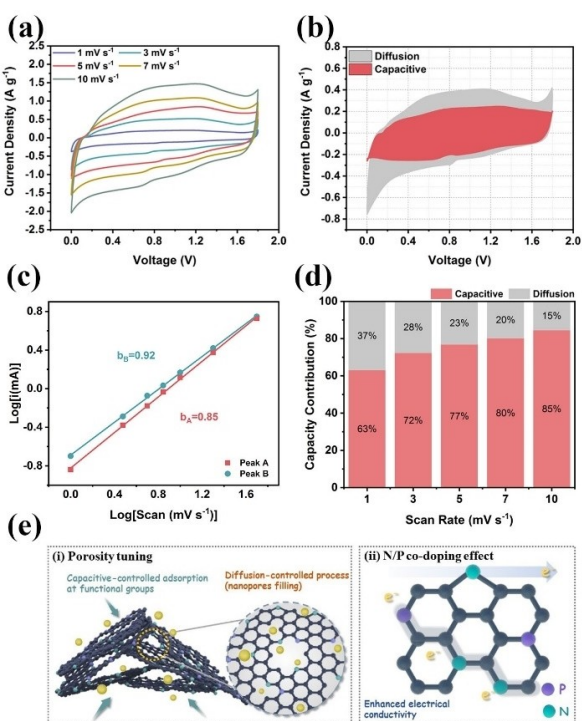


**Figure 6.** a) CV curves at scan rates from  $1 \text{ mV s}^{-1}$  to  $10 \text{ mV s}^{-1}$ ; b) capacitive contributions in CVs at a scan rate of  $1 \text{ mV s}^{-1}$ ; c)  $b$ -values analysis from fitting plot between  $\log(i)$  vs.  $\log(v)$ ; d) the ratios of capacitive and diffusive contributions at different scan rates ( $1 \text{ mV s}^{-1}$  to  $10 \text{ mV s}^{-1}$ ) of the GNPC-based ZICs. e) A schematic diagram showing the advantages of the GNPC, including the synergistic effect of porosity tuning and N,P-co-doping.

## Experimental Section

### Materials

Glucose, sodium hypophosphite ( $\text{NaH}_2\text{PO}_2$ ), melamine,  $\text{ZnSO}_4$ ,  $\text{Li}_2\text{SO}_4$  purchased from Sigma-Aldrich were used without further purification.

### Synthesis of porous carbon materials

Typically, glucose was mixed with  $\text{NaH}_2\text{PO}_2$  and melamine in a weight ratio of 1:1:4. After grinding for 30 min, the resulting uniform powder was transferred into a crucible and dried under vacuum at 80 °C for 1 h to remove adsorbed  $\text{H}_2\text{O}$ . Then the crucible was quickly put into a furnace with an argon atmosphere and heated to 300 °C for 2 h and then kept at 800 °C for another 2 h at a heating rate of 5 °C min<sup>-1</sup>. The resulting samples were collected and immersed in 1 M HCl solution for 48 h to remove inorganics and impurities, and then washed with water until the filtrate was neutral. The glucose-derived N,P-co-doped 2D carbon nanosheets were marked GNPC. The control samples also synthesized without  $\text{NaH}_2\text{PO}_2$  or melamine were named GNC and GPC. The glucose-derived carbon GC was prepared from directly carbonized glucose without any additives.

In addition, control experiments were conducted to reveal the effect of different  $\text{NaH}_2\text{PO}_2$  contents in the mixture on porosity of GNPC. In the experiment, the mass ratios of glucose, melamine and  $\text{NaH}_2\text{PO}_2$  were 1:1:2 and 1:1:6. The obtained carbon materials were marked GNPC-X.

### Characterization

Field-emission scanning electron microscopy (SEM, XL30ESEM-FEG) with an accelerating voltage of 20 kV and high-resolution transition electron microscopy (HRTEM, JEM-1011 at 200 kV) were employed to observe the morphology and nanostructure of all samples. XRD patterns were obtained on the D8 Advance X-ray diffractometer with  $\text{Cu K}_\alpha$  radiation at 60 kV and 60 mA. Raman spectra were collected using a Renishaw micro-Raman spectrometer (laser wavelength = 532 nm). X-ray photoelectron spectra (XPS, VG ESCALAB MK II spectrometer) were obtained with  $\text{Al K}_\alpha$  radiation at 10.0 kV and 10 mA. The structural properties were estimated by nitrogen adsorption/desorption at -196 °C on a Quantachrome Autosorb-1 C-MS analyzer. Brunauer-Emmett-Teller (BET) method and density function theory (DFT) were used to calculate the specific surface area (SSA) and pore size distribution (PSD) of the carbon materials, respectively.

### Electrochemical measurements

The electrochemical properties of the porous carbon materials, including supercapacitors (SCs) and zinc ion capacitors (ZICs), were tested with an electrochemical workstation EC-LAB VMP3 (BioLogic Science Instruments).

For SCs, the active materials, PTFE binder (5 wt%) and acetylene black at a weight ratio of 8:1:1 were mixed into a slurry for the working electrode (2 mg). The as-prepared electrodes were pressed onto a nickel foam ( $D=10$  mm) and dried in vacuum at 90 °C for 12 h to remove  $\text{H}_2\text{O}$ . After pressing at 10 MPa, two working electrodes were assembled with a separator (Whatman; GF/A, 13 mm diameter) in a Swagelock cell with aqueous 1 M  $\text{Li}_2\text{SO}_4$  electrolyte. The electrochemical performance of SC was examined by cyclic voltammetry (CV) and galvanostatic charge/discharge (GCD) measurements in the same voltage window from 0 to 1.8 V.

Furthermore, electrochemical impedance spectroscopy (EIS) measurements were carried out within the frequency range 100 kHz to 10 mHz. The specific capacitance ( $C_s$ ), energy ( $E$ , Wh kg<sup>-1</sup>) and power density ( $P$ , W kg<sup>-1</sup>) for a single electrode were calculated from GCD curves:

$$C_s = \frac{I\Delta t}{m\Delta V} \quad (4)$$

$$E = \frac{C\Delta V^2}{(8 \times 3.6)} \quad (5)$$

$$P = \frac{E}{\Delta t} \quad (6)$$

where  $I$  is the applied current (A),  $\Delta t$  is the discharge time (s),  $\Delta V$  is the voltage window, and  $m$  is the total mass of the active material on the working electrode (g).

The diffusion coefficient ( $D$ , cm<sup>2</sup> s<sup>-1</sup>) is calculated according to:<sup>[20a]</sup>

$$D = \frac{R^2 T^2}{2 A^2 n^4 F^4 C^2 \sigma^2} \quad (7)$$

where  $R$  is universal gas constant,  $T$  is the absolute temperature,  $A$  is the effective surface area between the electrolyte and sample,  $n$  is the number of electrons,  $F$  is the Faraday constant,  $C$  is the concentration of ions, and  $\sigma$  is the Warburg factor, which is related to  $Z'$ . Equation (5) relates the real part of impedance ( $Z'$ ) to the spreading resistance ( $R_s$ ), charge transfer resistance ( $R_{ct}$ ), and angular frequency ( $\omega$ ).<sup>[35]</sup>

$$Z' = R_s + R_{ct} + \sigma\omega^{-1/2} \quad (8)$$

For the ZICs, the slurry was prepared with the same ratio of glucose-derived porous carbon, PTFE binder (5 wt%) and acetylene black (8:1:1) in ethanol. After the evaporating excess solvent the remaining material was roll-pressed on grafoil, and then cut into small discs (10 mm diameter). The prepared electrodes were dried at 90 °C overnight, assembled with the anodic Zn metal foil (10 mm diameter) and separator (Whatman GF/F, 13 mm diameter) in a Swagelok cell with 2 M  $\text{ZnSO}_4$  aqueous electrolyte. The corresponding specific capacitance ( $C_s$ ) and energy ( $E$ , Wh kg<sup>-1</sup>) and power densities ( $P$ , W kg<sup>-1</sup>) for a single electrode are calculated as:<sup>[3]</sup>

$$C_s = \frac{I\Delta t}{m\Delta V} \quad (9)$$

$$E = \frac{C\Delta V^2}{(2 \times 3.6)} \quad (10)$$

$$P = \frac{E}{\Delta t} \quad (11)$$

where  $I$  is the applied current (A),  $\Delta t$  is the discharge time (s),  $\Delta V$  is the voltage window, and  $m$  is the total mass of the active material on the working electrode (g).

### Acknowledgements

The authors are grateful for the financial support from the NCN, Poland, UMO-2020/39/B/ST8/02937. The author would like to thank Professor Mirosława El Fray and Ms. Małwina Niedźwiedź from Department of Polymer and Biomaterials Science, Faculty of Chemical Technology and Engineering, West Pomeranian University of Technology in Szczecin for their help in the contact angle measurement.

## Conflict of Interests

The authors declare no conflict of interest.

## Data Availability Statement

Research data are not shared.

**Keywords:** porous carbon · zinc-ion capacitor · 2D nanosheets · N,P co-doping

- [1] a) J. Li, J. Zhang, L. Yu, J. Gao, X. He, H. Liu, Y. Guo, G. Zhang, *Energy Storage Mater.* **2021**, *42*, 705–714; b) Z. Cai, J. Wang, Y. Sun, *eScience* **2023**, *3*,100093; c) J. Li, L. Yu, Y. Li, G. Wang, L. Zhao, B. Peng, S. Zeng, L. Shi, G. Zhang, *Nanoscale* **2021**, *13*, 692–699; d) J. Li, L. Yu, W. Wang, X. He, G. Wang, R. Liu, X. Ma, G. Zhang, *J. Mater. Chem. A* **2022**, *10*, 9355–9362; e) J. Gao, G. Wang, W. Wang, L. Yu, B. Peng, A. El-Harairy, J. Li, G. Zhang, *ACS Nano* **2022**, *16*, 6255–6265.
- [2] P. Shang, M. Liu, Y. Mei, Y. Liu, L. Wu, Y. Dong, Z. Zhao, J. Qiu, *Small* **2022**, *18*, 2108057.
- [3] R. Yuksel, O. Buyukcakir, W. K. Seong, R. S. Ruoff, *Adv. Energy Mater.* **2020**, *10*, 1904215 .
- [4] W. Han, G. Liu, W. Seo, H. Lee, H. Chu, W. Yang, *Carbon* **2021**, *184*, 534–543.
- [5] a) L. Yang, X. He, Y. Wei, H. Bi, F. Wei, H. Li, C. Yuan, J. Qiu, *Nano Res.* **2022**, *15*, 4068–4075; b) S. Wang, T. Zhang, J. Li, Y. Hua, J. Dou, X. Chen, S. Li, *Environ. Sci. Eur.* **2023**, *35*, 1–12.
- [6] a) S. Saini, P. Chand, A. Joshi, *J. Energy Storage* **2021**, *39*, 102646; b) P. B. Naik, P. Yadav, R. Nagaraj, R. Puttaswamy, H. K. Beere, U. N. Maiti, C. Mondal, N. Sanna Kotrappanavar, D. Ghosh, *ACS Sustainable Chem. Eng.* **2022**, *10*, 1471–1481.
- [7] a) X. Zhu, F. Guo, Q. Yang, H. Mi, C. Yang, J. Qiu, *J. Power Sources* **2021**, *506*, 230224; b) M. Peng, L. Wang, L. Li, X. Tang, B. Huang, T. Hu, K. Yuan, Y. Chen, *Adv. Funct. Mater.* **2021**, *32*, 2109524.
- [8] C. C. Hou, Y. Wang, L. Zou, M. Wang, H. Liu, Z. Liu, H. F. Wang, C. Li, Q. Xu, *Adv. Mater.* **2021**, *31*, 2101698.
- [9] Y. G. Lee, J. Lee, G. H. An, *Adv. Funct. Mater.* **2021**, *31*, 2104256.
- [10] a) W. Zhang, M. Sun, J. Yin, K. Lu, U. Schwingenschlögl, X. Qiu, H. N. Alshareef, *Adv. Energy Mater.* **2021**, *11*, 2101928; b) Q. Chen, S. Wang, S. Li, A. Zhang, *J. Polym. Res.* **2022**, *30*, 32; c) S. Wang, W. Wu, Q. Chen, Z. Ding, S. Li, A. Zhang, T. Tang, J. Liu, P. U. Okoye, *J. Appl. Polym. Sci.* **2022**, *140*, 53430.
- [11] M. Liu, X. Li, C. Shao, C. Han, Y. Liu, X. Li, X. Ma, F. Chen, Y. Liu, *Energy Storage Mater.* **2022**, *44*, 250–262.
- [12] Z. Anfar, A. A. El Fakir, M. Zbair, Z. Hafidi, A. Amedlous, M. Majdoub, S. Farsad, A. Amjleff, A. Jada, N. El Alem, *Chem. Eng. J.* **2021**, *405*, 126660.
- [13] B. Liu, L. Ye, R. Wang, J. Yang, Y. Zhang, R. Guan, L. Tian, X. Chen, *ACS Appl. Mater. Interfaces* **2018**, *10*, 4001–4009.
- [14] a) H. Wang, H. Niu, H. Wang, W. Wang, X. Jin, H. Wang, H. Zhou, T. Lin, *J. Power Sources* **2021**, *482*, 228986; b) F. Wang, J. Y. Cheong, Q. He, G. Duan, S. He, L. Zhang, Y. Zhao, I.-D. Kim, S. Jiang, *Chem. Eng. J.* **2021**, *414*, 128767.
- [15] a) C. Li, X. Zhang, Z. Lv, K. Wang, X. Sun, X. Chen, Y. Ma, *Chem. Eng. J.* **2021**, *414*, 128781; b) Y. Lu, Z. Li, Z. Bai, H. Mi, C. Ji, H. Pang, C. Yu, J. Qiu, *Nano Energy* **2019**, *66*, 104132.
- [16] S. Zhang, M. Galinski, X. Liu, K. Sielicki, X. Chen, P. K. Chu, R. Holze, E. Mijowska, *Microporous Mesoporous Mater.* **2021**, *310*, 110629.
- [17] J. Li, B. Michalkiewicz, J. Min, C. Ma, X. Chen, P. K. Chu, J. Gong, E. Mijowska, T. Tang, *Chem. Eng. J.* **2019**, *360*, 250–259.
- [18] W. Fan, J. Ding, J. Ding, Y. Zheng, W. Song, J. Lin, C. Xiao, C. Zhong, H. Wang, W. Hu, *Nano-Micro Lett.* **2021**, *13*, 59.
- [19] a) J. X. Li, B. Michalkiewicz, J. K. Min, C. D. Ma, X. C. Chen, J. Gong, E. Mijowska, T. Tang, *Chem. Eng. J.* **2019**, *360*, 250–259; b) J. Li, X. Chen, J. Gong, J. Zhu, E. Mijowska, *Diamond Relat. Mater.* **2020**, *105*, 107802.
- [20] a) X. Liu, C. Ma, Y. Wen, X. Chen, X. Zhao, T. Tang, R. Holze, E. Mijowska, *Carbon* **2021**, *171*, 819–828; b) Y. Wen, X. Liu, X. Wen, X. Chen, K. Szymańska, R. Dobrýnska, E. Mijowska, *Compos. B. Eng.* **2020**, *199*, 108256.
- [21] Y. Wen, X. Chen, E. Mijowska, *Chemistry* **2020**, *26*, 16328–16337.
- [22] S. Zhang, X. Shi, R. Wróbel, X. Chen, E. Mijowska, *Electrochim. Acta* **2019**, *294*, 183–191.
- [23] H. Zhou, S. Wu, H. Wang, Y. Li, X. Liu, Y. Zhou, *J. Hazard. Mater.* **2021**, *402*, 124023.
- [24] M. Yi, B. Lu, X. Zhang, Y. Tan, Z. Zhu, Z. Pan, J. Zhang, *Appl. Catal. B* **2021**, *283*, 119635.
- [25] a) M. Shang, J. Zhang, X. Liu, Y. Liu, S. Guo, S. Yu, S. Filatov, X. Yi, *Appl. Surf. Sci.* **2021**, *542*, 148697; b) A. R. Selvaraj, A. Muthusamy, C. Inho, H.-J. Kim, K. Senthil, K. Prabakar, *Carbon* **2021**, *174*, 463–474.
- [26] Z. Chen, S. Zhao, H. Zhao, Y. Zou, C. Yu, W. Zhong, *Chem. Eng. Eng. J.* **2021**, *409*, 127891.
- [27] L. Fu, Q. Qu, R. Holze, Y. Wu, *J. Solid. State Electr.* **2019**, *23*, 717–724.
- [28] S. Zhang, X. Shi, D. Moszyński, T. Tang, P. K. Chu, X. Chen, E. Mijowska, *Electrochim. Acta* **2018**, *269*, 580–589.
- [29] X. Liu, Y. Wen, X. Chen, A. Dymerska, R. Wróbel, J. Zhu, X. Wen, Z. Liu, E. Mijowska, *ACS Appl. Energ. Mater.* **2020**, *3*, 8562–8572.
- [30] H. Wang, M. Wang, Y. Tang, *Energy Storage Mater.* **2018**, *13*, 1–7.
- [31] a) L. Lei, Y. Zheng, X. Zhang, Y. Su, X. Zhou, S. Wu, J. Shen, *Chem. Asian J.* **2021**, *16*, 2146–2153; b) X. Fan, P. Liu, B. Ouyang, R. Cai, X. Chen, X. Liu, W. Liu, J. Wang, K. Liu, *ChemElectroChem* **2021**, *8*, 3572–3578; c) Y. Zhao, H. Hao, T. Song, X. Wang, C. Li, W. Li, *J. Power Sources* **2022**, *521*, 230941; d) L. Yan, T. Liu, X. Zeng, L. Sun, X. Meng, M. Ling, M. Fan, T. Ma, *Carbon* **2022**, *187*, 145–152; e) G. Sun, H. Yang, G. Zhang, J. Gao, X. Jin, Y. Zhao, L. Jiang, L. Qu, *Energy Environ. Sci.* **2018**, *11*, 3367–3374; f) J. Wang, B. Zhang, Z. Cai, R. Zhan, W. Wang, L. Fu, M. Wan, R. Xiao, Y. Ou, L. Wang, J. Jiang, Z. W. Seh, H. Li, Y. Sun, *Sci. Bull.* **2022**, *68*, 716–724; g) Y. Zheng, W. Zhao, D. Jia, Y. Liu, L. Cui, D. Wei, R. Zheng, J. Liu, *Chem. Eng. J.* **2020**, *387*, 124161; h) Z. Li, D. Chen, Y. An, C. Chen, L. Wu, Z. Chen, Y. Sun, X. Zhang, *Energy Storage Mater.* **2020**, *28*, 307–314; i) Y. G. Lee, G. H. An, *ACS Appl. Mater. Interfaces* **2020**, *12*, 41342–41349; j) C. Liu, J. C. Wu, H. Zhou, M. Liu, D. Zhang, S. Li, H. Gao, J. Yang, *Molecules* **2019**, *24*, 2589.
- [32] a) J. Zeng, L. Dong, L. Sun, W. Wang, Y. Zhou, L. Wei, X. Guo, *Nano-Micro Lett.* **2020**, *13*, 19; b) D. Wang, Z. Pan, G. Chen, Z. Lu, *Electrochim. Acta* **2021**, *379*, 138170; c) G. Lou, G. Pei, Y. Wu, Y. Lu, Y. Wu, X. Zhu, Y. Pang, Z. Shen, Q. Wu, S. Fu, H. Chen, *Chem. Eng. J.* **2021**, *413*, 127502; d) P. Yu, Y. Zeng, Y. Zeng, H. Dong, H. Hu, Y. Liu, M. Zheng, Y. Xiao, X. Lu, Y. Liang, *Electrochim. Acta* **2019**, *327*, 13499; e) M. Z. Iqbal, M. M. Faisal, M. Sulman, S. R. Ali, A. M. Afzal, M. A. Kamran, T. Alharbi, *J. Energy Storage* **2020**, *29*, 101324; f) P. Liu, W. Liu, Y. Huang, P. Li, J. Yan, K. Liu, *Energy Storage Mater.* **2020**, *25*, 858–865; g) Z. Liu, G. Li, T. Cui, A. Borodin, C. Kuhl, F. Endres, *J. Solid State Electrochem.* **2017**, *22*, 91–101.
- [33] X. Jin, L. Song, C. Dai, Y. Xiao, X. Li, Y. Wang, J. Zhang, Y. Zhao, Z. Zhang, N. Chen, L. Jiang, L. Qu, *Adv. Mater.* **2022**, *34*, 2109450.
- [34] S. Wu, Y. Chen, T. Jiao, J. Zhou, J. Cheng, B. Liu, S. Yang, K. Zhang, W. Zhang, *Adv. Energy Mater.* **2019**, *9*, 1902915.
- [35] H. Tian, J. Qin, D. Hou, Q. Li, C. Li, Z. S. Wu, Y. Mai, *Angew. Chem. Int. Ed.* **2019**, *58*, 10173–10178.

Manuscript received: April 25, 2023

Revised manuscript received: June 25, 2023

Accepted manuscript online: July 2, 2023

Version of record online: July 11, 2023